energies

MDPI

Article

Revealing the NO Formation Kinetics for NH_3/CH_4 Blends Under Dual-Flame and Premixed Swirl Flame Configurations

Siqi Wang [1], Cheng Tung Chong [1,*], Soroush Sheykhbaglou [1], Jo-Han Ng [2], Bo Tian [3] and Agustin Valera-Medina [4]

[1] China-UK Low Carbon College, Shanghai Jiao Tong University, Lingang, Shanghai 201306, China; siqi_wang@sjtu.edu.cn (S.W.); soroush.sheykhbaglou@sjtu.edu.cn (S.S.)
[2] Carbon Neutrality Research Group, University of Southampton Malaysia, Iskandar Puteri 79100, Johor, Malaysia; j.ng@soton.ac.uk
[3] School of Engineering, University of Leicester, Leicester LE1 7RH, UK
[4] College of Physical Sciences and Engineering, Cardiff University, Cardiff CF24 3AA, UK; valeramedinaa1@cardiff.ac.uk
* Correspondence: ctchong@sjtu.edu.cn

Abstract: Ammonia stands out as a promising zero-carbon fuel and an efficient hydrogen carrier, offering great promise for industrial applications in gas turbines and boilers. However, different combustion modes significantly influence the flame structure and combustion characteristics of ammonia. In this study, two distinct fuel injection strategies were employed in a model combustor: ammonia and methane, under fully premixed and dual-flame combustion modes. Numerical simulations were performed to analyze the flame structure, velocity fields, and temperature distribution, complemented by planar flow field, flame OH* chemiluminescence, and NO emission measurements. Findings reveal that with an increasing NH_3 ratio, the flame front becomes more elongated with more pronounced temperature fluctuations at the swirler exit. Particularly, at 50% NH_3, a significant reduction in flame temperature is observed, notably at a height of 30 mm from the burner. For dual flames, the reaction $NH_2 + O \leftrightarrow HNO + H$ was less significant compared to its effect in premixed flames, whereas the $H + O_2 \leftrightarrow O + OH$ reaction demonstrated the highest sensitivity coefficient. An increase in the NH_3 ratio correspondingly led to a reduction in NO consumption reaction rates, heightening the sensitivity coefficient for NO inhibition, and providing critical insights into ammonia combustion optimization.

Keywords: ammonia; swirl flame; PIV; dual flame; FGM model; NO_x emissions

Citation: Wang, S.; Chong, C.T.; Sheykhbaglou, S.; Ng, J.-H.; Tian, B.; Valera-Medina, A. Revealing the NO Formation Kinetics for NH_3/CH_4 Blends Under Dual-Flame and Premixed Swirl Flame Configurations. *Energies* **2024**, *17*, 6090. https://doi.org/10.3390/en17236090

Academic Editor: Qiongyao Qin

Received: 12 October 2024
Revised: 18 November 2024
Accepted: 28 November 2024
Published: 3 December 2024

1. Introduction

Ammonia has gained significant attention from the global community as a potential zero-carbon, environmentally clean fuel in response to the growing concerns regarding the proliferation of fossil fuel consumption and carbon emissions [1]. In contrast to hydrogen, ammonia has undergone extensive investigation as a hydrogen storage medium for renewable energy, owing to its relative ease of liquefaction and straightforward storage and transportation solutions. This advantage addresses the complex challenges associated with the storage and transportation of hydrogen [2]. Moreover, the clean combustion of ammonia is distinguished by the exclusive production of water and nitrogen as byproducts, eliminating carbon emissions and presenting a cleaner alternative to traditional fuels.

Nevertheless, despite the promising potential of ammonia in the energy sector, its practical application encounters some significant challenges, including the high level of nitrogen oxide (NO_x) emissions due to the fuel-bound nitrogen, unstable combustion owing to low reactivity, difficulty in ignition, among others [3]. Jójka et al. [4] investigated the emission characteristics of methane-air swirl premixed flames with ammonia addition using CFD (Fluent) and Chemkin simulations. The experiments were conducted at constant

burner powers of 15 and 30 kW with an equivalence ratio of 0.71. The fuel composition ranged from 0.0–5.0% NH_3 (balance CH_4) with an inlet temperature of 473 K and mass flow rate recirculation ratios of 0–0.4. The results indicated that with a 5% NH_3 addition, the burner with an outflow angle of 30° exhibited the lowest NO emissions (1585 ppmv), comparable to the NO emissions when the fuel power was doubled. For the SW30 burner, the central recirculation zone diameter was 12 cm, correlating with a significant increase in temperature and NO concentration. Additionally, the presence of the outer recirculation zone extended the residence time and reduced local temperatures near the wall due to heat losses, thereby lowering the final NO concentration. Effectively addressing the reduction in NO_x emissions remains a pivotal concern, prompting ongoing research efforts by numerous scholars in the field.

An et al. [5] investigated the emission characteristics of CH_4/NH_3/air premixed swirl flames, with a maximum NH_3 mole fraction of 60%. By combining Large Eddy Simulation (LES) with the Flame Generated Manifold (FGM) model, the study identified nitrogen-containing species, residence time, and temperature as key factors influencing NO concentration distribution. NO is primarily formed in the inner recirculation zone, and the distribution of OH and NO in the premixed CH_4/NH_3/air flames is correlated. HNO plays a major role in NO formation, with NO emission peaking when the NH_3 ratio approaches 40%. Similarly, Xiao et al. [6] investigated the co-combustion of ammonia and methane under gas turbine conditions, comparing five different detailed reaction mechanisms. They also employed a chemical reactor network (CRN) model for 1D simulations, comparing scenarios at different pressures of 1.0 atm and 2.0 atm, and analyzed various equivalence ratios, ranging from lean to rich mixtures. The study results indicate that, in gas turbines, slightly fuel-rich combustion can effectively reduce NO_x emissions; therefore, under fuel-rich conditions, the Tian mechanism [7] was employed as an appropriate model for studying ammonia/methane combustion. Although other mechanisms such as Okafor [8] have demonstrated good performance for these blends, the latter is based on Tian's mechanism, hence increasing confidence in its selection at the time. Additionally, increasing pressure during ammonia/methane combustion suppresses NO_x formation, significantly lowering NO_x emissions, with the NH + OH ↔ HNO + H reaction being the most influential for NO conversion under high pressure, further highlighting its importance. Furthermore, higher combustion chamber inlet temperatures help reduce NO_x generation, making temperature control crucial for NO_x management. Moreover, under gas turbine combustion conditions, the oxidation reactions of HNO and N are the primary pathways for NO formation, indicating that these reactions are critical for NO_x emissions.

Ahmed et al. [9] have summarized the latest advancements in experimental and numerical simulations of stable, low-emission ammonia combustion burners. Studies show that mixing ammonia with high-reactivity fuels (such as H_2 and CH_4) can enhance flame stability and extend the operational range of burners, but it may also lead to increased NO emissions. In premixed flame burners, the combination of high-reactivity fuels with ammonia improves flame stability. However, this mixture tends to increase NO emissions due to the elevated concentration of free radicals (such as H and OH), and this effect is more pronounced when the mixture becomes leaner. One alternative is to use stratified fuel injection via dual injection. Mashruk et al. [10] showed that by stratification of the fuel via central swirl injection, it was possible to mitigate NO_x emissions from ammonia/hydrogen blends, a process that occurs due to the additional recombination of species at the flame front of the main flame. This concurs with our preceding work which showed that the dual-fuel injection method, i.e., a central pilot ammonia premixed jet flame surrounded by an outer swirl flame, forms a stratified flame which showed a reduction in NO by a factor of two compared to fully premixed flame [11]. Preheating the air for the dual-fuel injection case leads to enhanced generation of NH_2 radicals due to NH_3 decomposition, resulting in further NO reduction via the reaction NH_2 + NO ↔ NNH + OH [12], highlighting the potential of NO reduction using such fuel injection technique.

In dual-swirl burners, co-combustion of ammonia-rich flames with methane-lean mixtures can effectively reduce NO emissions. This approach maintains the overall mixture equivalence ratio on the lean ammonia flame side to ensure high combustion efficiency while preventing ammonia from being emitted into the exhaust. Furthermore, in dual-swirl burners, increasing the methane fraction in the external mixing stream significantly reduces NO emissions. This is because the increase in methane reduces the concentrations of O, OH, and H radicals near the internal NH_3 flame and shifts the overall mixture equivalence ratio from the lean side toward the stoichiometric side, thereby helping to reduce NO formation. Concurrently, Ji et al. [13] conducted a study on the lean premixed NH_3/CH_4/air flames with swirl combustion, employing simultaneous PIV/OH-PLIF measurements to obtain flow field and instantaneous OH distribution data. The results indicated that NH_3/air flames exhibit a blunter flame front and are prone to excessive stretching, which can lead to local extinction, thereby resulting in relatively poor stability. However, mixing methane with ammonia creates more wrinkles in the flame front, significantly enhancing the flame's resistance to stretch-induced extinction. Moreover, the addition of methane not only increases the laminar flame speed, maximum heat release rate, and adiabatic flame temperature but also collectively improves the flame stability.

Conversely, researchers like Zhang et al. [14] conducted experimental and numerical studies on ammonia/methane co-firing in swirl burners, analyzing extinction and flame macrostructure. The research indicates that, due to weaker combustion, NH_3 flames exhibit significantly poorer stability limits compared to CH_4 flames under lean flame conditions, suggesting that ammonia flames are more prone to extinction in lean mixtures. However, the addition of 50% CH_4 can significantly extend the extinction limit ϕ, and further increasing the swirl number with this mixture component can enhance the extinction limit even more, demonstrating the substantial improvement in flame stability provided by methane. Additionally, numerical results reveal that the extinction process of NH_3 flames occurs more rapidly compared to CH_4 flames, and excessive stretching has a more pronounced impact on local extinction in NH_3 flames.

In summary, despite considerable advancements in ammonia combustion on a global scale, there remains a critical need to delve deeper into specific parameters governing this process. Although ammonia/hydrogen is the net zero blend of excellence, the practical operation of industrial systems is likely to occur between ammonia and fossil fuels, hence ensuring a smoother transition towards decarbonization. Thus, ammonia/methane blends are a critical path towards a complete net zero future. This fact requires a comprehensive investigation into various combustion methods and strategies to achieve the dual objective of improving combustion efficiency and reducing NO_x emissions more effectively when using these blends. This study aims to provide a thorough examination of the dual flame characteristics and premixed combustion of ammonia through a combined approach of experimental analysis and numerical simulations.

The methodology incorporates the introduction of ammonia and air through jet injection, while methane and air are introduced through a swirl method to achieve their combined combustion within the chamber. Particle imaging velocimetry (PIV) is used to analyze the flow velocity field of the flame, providing validation data for the numerical simulations. In terms of numerical modeling, the study employs the FGM model to ensure consistency across both combustion strategies regarding grids, boundary conditions, initial values, and computational settings. Furthermore, the study utilizes Chemkin for numerical simulations of the CRN model, analyzing the sensitivity of NO under different NH_3/CH_4 percentages as well as the mole fractions of OH, NO_2, N_2O, and NO.

2. Experimental Setup and Methodology

2.1. Swirl Flame System

The swirl burner utilized in this experimental setup comprises a high temperature-resistant square quartz window (80 × 80 mm) and a swirler, constructed from 304 stainless steel. The swirl component features eight straight vanes set at a 45-degree angle. The

swirl number (S_N), a crucial parameter, is calculated using Equation (1). Here, D_h and D_s denote the diameters of the swirler hub and the diameter of the swirler, respectively, while θ represents the angle between the swirl vanes and the center line. The calculated swirl number for this burner is 0.79, indicating a high swirl ($S_N > 0.6$), contributing significantly to flame stabilization.

$$S_N = \frac{2}{3}\left[\frac{1-(D_h/D_s)^3}{1-(D_h/D_s)^2}\right] tan\,\theta \quad (1)$$

The experimental design encompasses two distinct combustion modes, namely premixed flame and dual flame combustion, employing a swirling combustion platform illustrated in Figure 1. In the dual flame combustion mode, precise air control is achieved through the utilization of two flow meters. The central circular orifice delivers a mixture of ammonia and air, while the outer section (coflow section) supplies a swirling flow of methane/air mixture. Consequently, two distinct flow passages are formed during combustion, with the dual flame serving as a stabilizing factor. The gaseous fuels and air are regulated by mass flow controllers (Sevenstar CS200, Qixing Huachuang Flow Meter Co., Ltd., Beijing, China), with an accuracy of ±1.0% of the full-scale range.

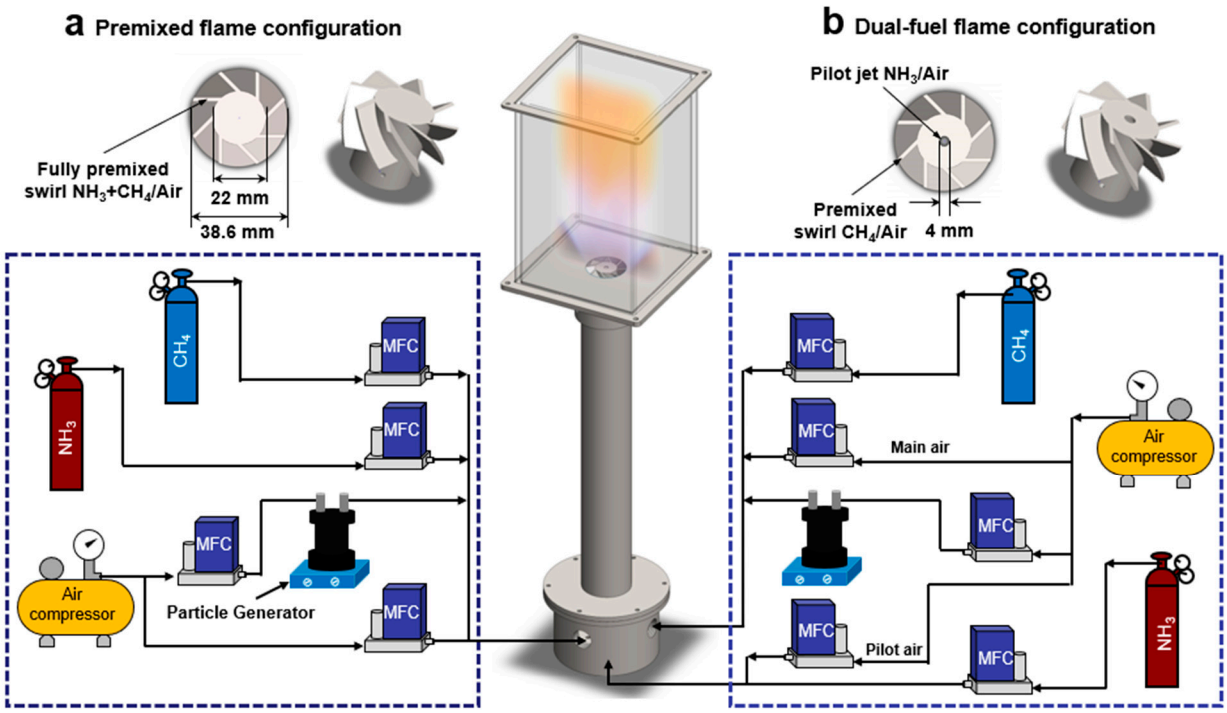

Figure 1. System diagram of swirl combustion platform for (**a**) Premixed and (**b**) Dual flame configurations [12].

2.2. Flame Structure, Flow Field and Emissions Measurements

Flame chemiluminescence of OH* and NH_2* was captured using a CCD camera (LaVision Imager SX 4M, LaVision GmbH, Göttingen, Germany) coupled with an image intensifier (LaVision IRO X, LaVision GmbH, Germany). The CCD camera operated at a resolution of 2360 × 1776 pixels, with a frame rate of 30 Hz and an exposure time of 8 ms. The IRO X, equipped with an 85 mm Nikon lens (Nikon Corporation, Tokyo, Japan), was positioned in front of the camera. A narrowband filter centered at 308 nm ± 5 nm was employed for OH* detection, while a filter at 630 nm ± 10 nm was used for NH_2* chemiluminescence imaging. For each flame, 150 images were acquired and averaged for analysis, followed by an Abel inversion to derive the spatial distribution of the chemiluminescence signal. Additionally, high-resolution images of the flames were obtained using a Sony A35 DSLR camera (Sony Corporation, Tokyo, Japan) with a 1/320 s exposure time.

In a flow field measurement experiment, a PIV system was employed, consisting of a tracer particle generator, laser system, CCD camera, and image post-processing system. The experiments utilized a two-dimensional PIV system (Lavision FlowMaster 2D, LaVision GmbH, Germany) to assess the flow field within a combustion chamber at a repetitive frequency of 15 Hz. Preliminary theoretical calculations guided the selection of a time interval (Δt) of 300 µs between two frames to ensure the acquisition of clearer high-contrast images. The laser system, operating at an average output pulse energy of 50 mJ/pulse, featured a wavelength of 532 nm, and a laser pulse width of 10 ns. The CCD camera (LaVision Imager SX 4M), vertically positioned on a 0.5 mm-thick laser sheet, was employed to illuminate titanium dioxide tracer particles with diameters ranging from 5 to 10 nm and densities of 3.9–4.2 g/cm^3. Subsequently, the LaVision Davis algorithm was applied for vector field computation. The final interpolation pixel setting was configured at 48 × 48 pixels with a 50% overlap. Precision in axial and radial velocity measurements was approximately ±2% of the full scale [15].

Post-combustion emission measurements were conducted via a KANE 9206 Quintox gas analyzer (Kane International Ltd., Welwyn Garden City, UK) to measure NO, using an 80 × 80 × 350 mm stainless steel cylinder on the top of the combustion chamber. The cross-section of the flue gas pipe was further reduced to 50 mm to enable single-point sampling after the flame was stabilized. The sampling flow rate was 2 L/min through a 5 mm diameter inlet. Each measurement took 180 s to ensure the reading was stabilized. The specifications and accuracy of the gas analyzer are as follows: Nitric oxide (NO) is measured in the range of 0–5000 ppm, with an accuracy of ±5 ppm or ±5%.

2.3. Operating Conditions

Table 1 summarizes the experimental conditions, distinguishing between two flame configurations: premixed flame and dual flame. The primary differences between these combustion modes lie in the mixing of fuel and oxygen and the resulting flame structure. In the dual-fuel flame, precise control over the mixing of different fuels and air is achievable. Experiments were conducted at ambient temperature and pressure. To stabilize the flame and measure emissions across a broader range of equivalence ratios, particularly in the fuel-lean region, emission measurements were performed at an equivalence ratio of ϕ = 0.7 with NH_3 volume fractions of 10%, 30%, and 50%. Detailed conditions for each experimental segment are comprehensively presented in Table 1.

Table 1. Experimental and numerical simulation conditions.

NH_3:CH_4 (v/v%)	Main Swirl Air Mass Flow Rate (g/s)	Methane Mass Flow Rate (g/s)	ϕ_{out}	Pilot Air Mass Flow Rate (g/s)	Ammonia Mass Flow Rate (g/s)	ϕ_{in}	Stratification Ratio (ϕ_{in}/ϕ_{out})	Global ϕ	Power (kW)
Premixed									
10/90	2.586	0.101	/	/	0.012	/	/	0.70	5.269
30/70	2.586	0.090	/	/	0.041	/	/	0.69	5.253
50/50	2.586	0.080	/	/	0.086	/	/	0.73	5.606
Dual flame									
10/90	2.155	0.101	0.80	0.431	0.012	0.17	0.21	0.70	5.269
30/70	2.155	0.090	0.71	0.431	0.041	0.58	0.82	0.69	5.253
50/50	2.155	0.080	0.64	0.431	0.086	1.21	1.89	0.73	5.606

2.4. Numerical Simulation

In this study, a three-dimensional model was developed using SolidWorks 2024 software, with the combustion chamber dimensions set at 80 × 80 × 350 mm. To ensure precise numerical simulations, the model was meshed using the Fluent Meshing tool within the ANSYS 2022 R2 platform. Subsequently, the numerical simulations were conducted using

ANSYS Fluent 2022 R2, providing a robust computational framework for analyzing fluid dynamics and combustion phenomena with high accuracy. The schematic diagram of the grid division for the 3D model is shown in Figure 2.

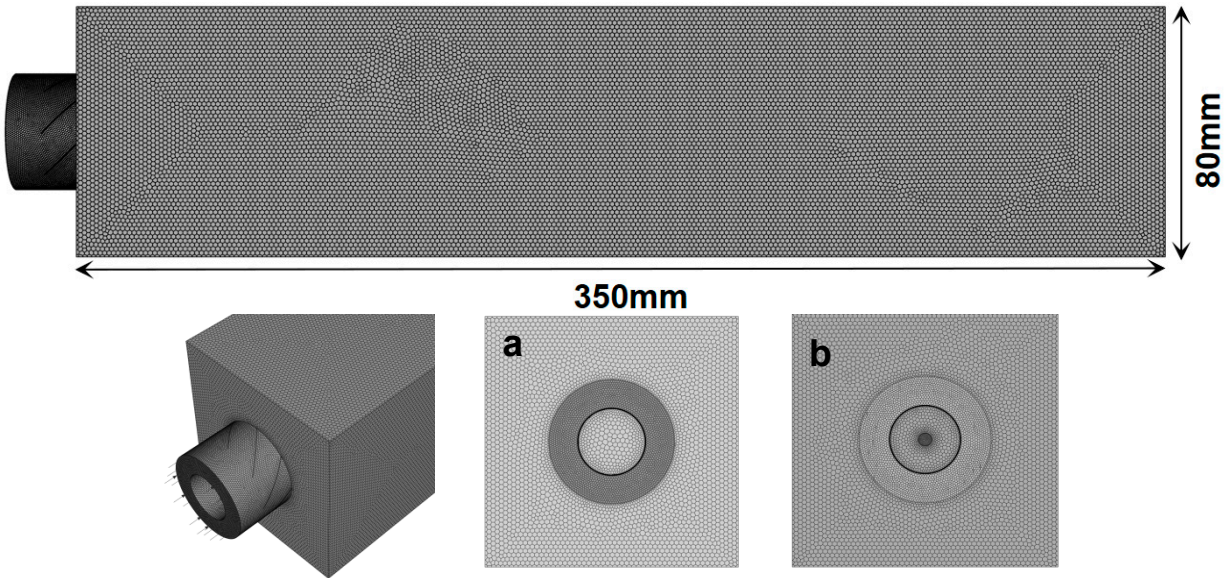

Figure 2. Grid partitioning of the 3D model, (**a**) premixed flame model and (**b**) dual flame model.

For the purposes of this investigation, the steady-state k-ω SST turbulence model was employed for simulation. The SST (Shear Stress Transport) model combines the advantages of the ω model and ε models to enhance the predictive performance of turbulence and viscous flow [16]. In this numerical simulation, the 'Mixed Type' wall heat boundary conditions, combining convective and radiative heat transfer were applied to model wall heat transfer more accurately, incorporating the effect of wall conduction. The heat transfer coefficient values were determined based on experimental data and empirical formulas recommended in the literature. Initial estimates of the thermal conductivity and convective heat transfer coefficients were made according to the flow characteristics, temperature distribution, and gas flow rates within the combustion chamber, then calibrated against experimental data from similar combustion devices to ensure the accuracy and reliability of the setup [17]. Furthermore, pressure interpolation employed the "Standard Format" method in Fluent, using linear interpolation between discrete mesh nodes to maintain stability and accuracy in the pressure field. Second-order upwind schemes were applied for the momentum, turbulent kinetic energy, turbulent dissipation rate, species conservation, and energy equations, while pressure-velocity coupling was solved using the SIMPLE algorithm.

Combustion simulations in this study utilized a partially premixed combustion model, which assumes the flame surface to be infinitely thin and describes unburned, burned, and intermediate states by introducing reaction progress variables [18]. The non-adiabatic small flame FGM model was adopted. This model offers an effective approach to characterize rapid chemical reactions [19]. As a non-adiabatic small flame model, the FGM model demonstrates significant advantages in handling rapid combustion reactions. Its core concept decomposes the flame structure into a series of steady-state flamelets, each representing a chemical reaction pathway. This approach allows the simulation of complex combustion processes by combining different flamelets, thus avoiding the time-consuming resolution of detailed chemical mechanisms. Compared to other models, the FGM model more effectively captures the non-uniformity and rapid combustion characteristics of flames, leading to more accurate and reliable simulations of partially premixed flames [20]. The reaction mechanism selected was Okafor's detailed mechanism [8], which covers 59 species and 356 elementary reactions. The Okafor mechanism is optimized and expanded based on the

GRI-3.0 mechanism [21] and Tian mechanism [7]. Table 2 tabulates the detailed parameter settings used for the numerical simulation.

Table 2. Simulation settings and parameters.

Simulation Parameters	Value Setting
Turbulence model	k-ω SST
Wall heat boundary conditions	Mixed type
Heat transfer coefficient of mixer wall	9.7 W/m^2·K [17]
Heat transfer coefficient of combustion chamber wall	13.44 W/m^2·K [17]
Pressure interpolation	Standard format
Equation format	Second-order upwind scheme
Pressure-velocity coupling solution method	SIMPLE algorithm
Combustion model	FGM model

This study focuses on the grid independence verification of different grid densities (430 k, 820 k, 1.6 M, and 2.5 M grids), with specific results shown in Figure 3, depicting cross-sectional temperature and velocity curves at a height of 20 mm. Although the temperature and velocity trends are nearly identical across the four grid densities, some errors are non-negligible. A convergence analysis was conducted to examine the simulation results under different grid densities. At grid densities of 430 k and 820 k, the simulation results showed unsatisfactory convergence, primarily due to insufficient grid resolution. However, when the grid density was increased to 1.6 M, the simulation results significantly improved and demonstrated good convergence, with clear distributions of temperature and velocity contours. Although a grid density of 2.5 M may offer higher resolution, it comes with increased computational costs. Based on this observation, a grid cell count of 1,600,000 was selected as optimal, providing a balance between simulation accuracy and computational efficiency. Consequently, 1,587,619 grid cells were chosen for premixed flame simulation and 1,640,945 grid cells for dual flame simulation.

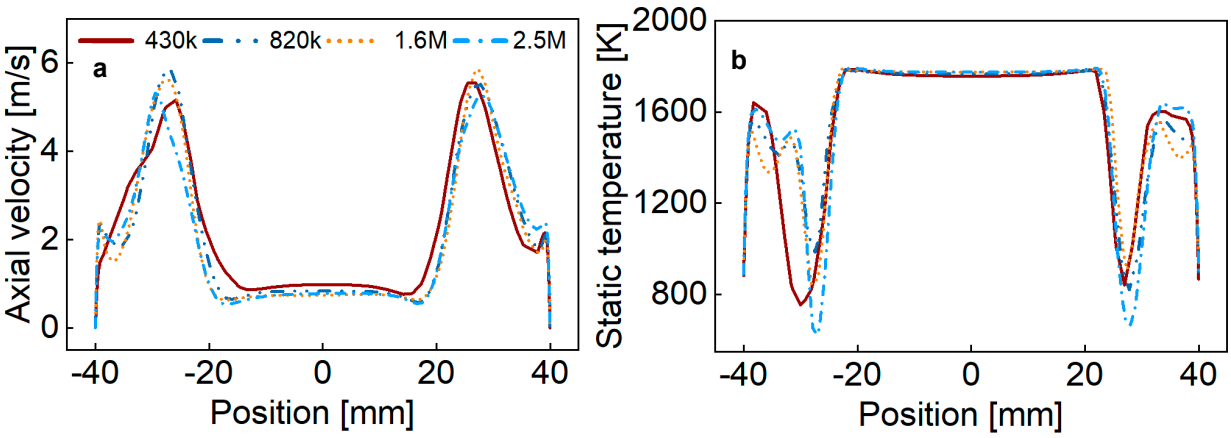

Figure 3. Comparison of (**a**) axial velocity and (**b**) static temperature profiles at a height of 20 mm for various grid densities.

The CRN model was employed to simulate the experimentally observed flames, combining perfectly stirred reactor (PSR) and plug flow reactor (PFR) models to capture the fluid dynamics and mixing characteristics in a swirl combustor. Figure 4 illustrates the CRN model for premixed and dual-fuel flames, which includes mixing, reaction, recirculation, and post-flame zones. The model was developed with ANSYS Chemkin 2022 R2. The premixed section utilized four PSR models and divided the recirculation zone into the external recirculation zone (ERZ) and the central recirculation zone (CRZ), with an 80 mm-long PFR simulating the premixed part. The reaction pathway and NO sensitivity analysis points were positioned at the PFR outlet, where the reaction was complete and aligned

with the experimental results. In the model, 70% of the flow proceeds to the post-flame zone, while 30% enters the recirculation zone, with 5% to the ERZ and 25% to the CRZ [22]. Numerical simulations were conducted under specified initial pressure and temperature conditions, using adiabatic conditions to simulate the absence of heat loss. The model calculated the average residence time of 0.5 ms based on empirical flow data. This study employed the reaction mechanism by Okafor et al. [8], previously described and that has been validated through a series of NH_3/CH_4/air and NH_3/H_2/air experiments [23]. Additionally, the study compared simulated and experimental NO emissions for NH_3/CH_4 mixtures at an equivalence ratio of 0.7 across different volume ratios.

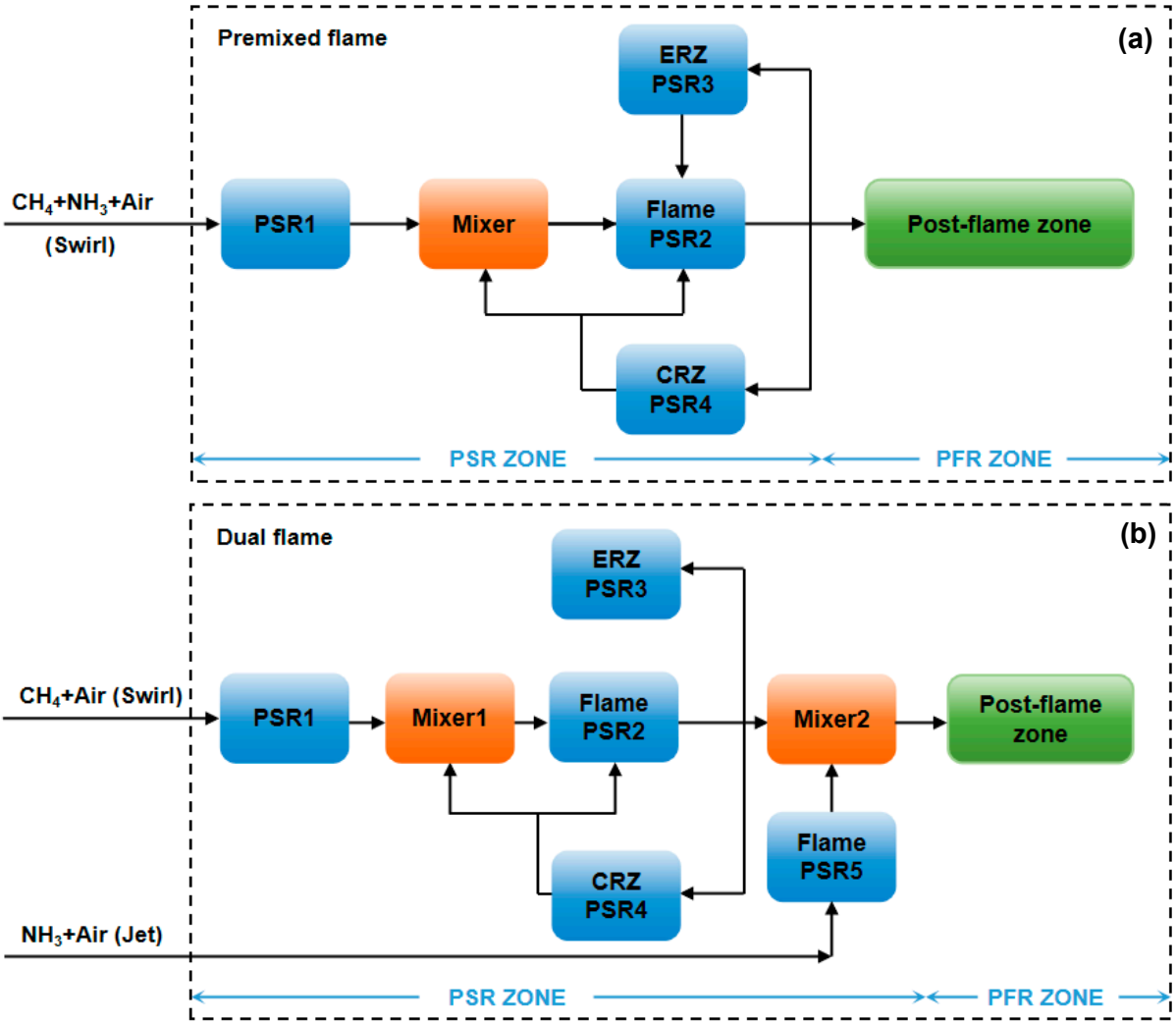

Figure 4. Schematic diagram of one-dimensional simulation of (**a**) premixed and (**b**) dual-fuel flames using a CRN model [12].

3. Results and Discussion

3.1. Flame Structure and Temperature Field

Figure 5 presents the direct images of the premixed flame alongside the OH* chemiluminescence and CFD simulation results for the OH mass fraction distribution. It is important to emphasize that the system measures only excited-state OH, i.e., OH*, which is primarily generated through the following two reactions [12], $CH + O_2 \rightarrow CO + OH^*$ (R1), $H + O + M \rightarrow OH^* + M$ (R2). When the proportion of CH_4 is higher, the probability of reaction (R1) occurring increases. In contrast, reaction (R2) is independent of the fuel type; although it is a three-body reaction, its probability of occurring under atmospheric conditions is relatively low. Therefore, the distribution of OH* may differ from that of OH.

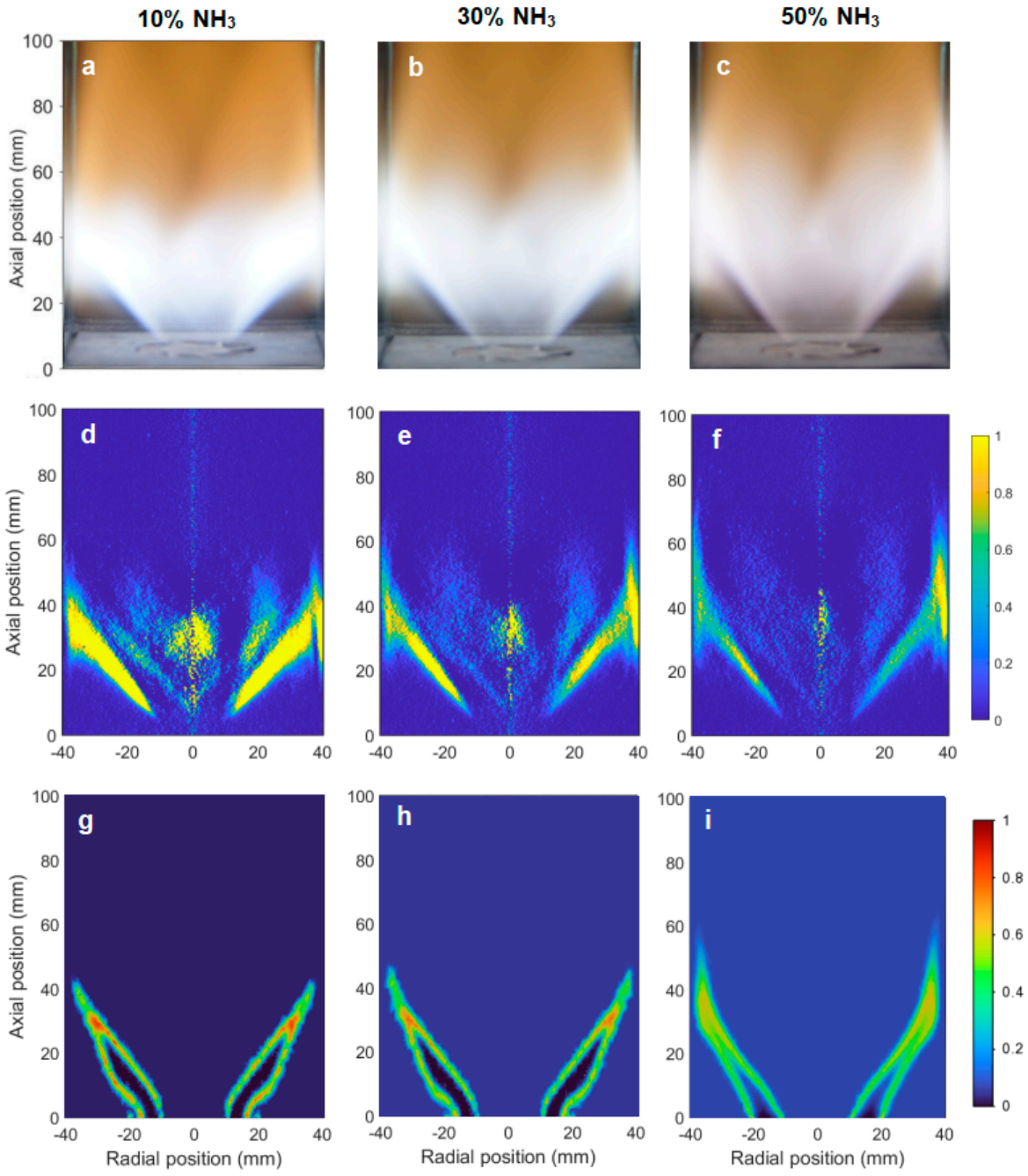

Figure 5. Premixed flame images (**a**–**c**) and OH* Abel inversion results (**d**–**f**) and CFD simulated OH mass fraction contour (**g**–**i**), ϕ = 0.7, with different NH_3/CH_4 vol.%.

As the NH_3 ratio increases, the flame height gradually rises, and the flame color transitions from bright orange-blue to a more diluted appearance. This is also evident from the OH* chemiluminescence and OH mass fraction distribution, where the weakening of flame intensity and noticeable changes in flame morphology are observed. Particularly at the outer edge and tip of the flame, the OH signal progressively weakens, and the flame structure begins to disappear at the root, indicating that the flame stability is affected. Meanwhile, the flame anchor point also changes. At higher NH_3 ratios, the flame no longer remains stably anchored at the burner outlet as it does at lower NH_3 ratios, but instead relies on swirl to maintain flame stability. This trend is clearly reflected in the change in flame morphology. As shown in Figure 5a–c, with the increase in the NH_3 ratio, the flame structure shows a tendency to elongate, and the flame tip height increases. This

change is consistent with the OH distribution, reflecting the evolution of the flame under different fuel ratios. In particular, when the NH_3 ratio reaches 50%, the flame height and length significantly increase, and the intensity of OH chemiluminescence decreases, further confirming the relationship between flame stability and fuel mixture ratio.

Figure 6 shows the actual images of the dual flames, alongside the OH* chemiluminescence and the corresponding CFD simulation results for the OH mass fraction distribution. It is evident that as the NH_3 percentage increases, the central jet NH_3 flame intensifies, while the swirl flame gradually weakens, resulting in an elongated V-shaped flame structure.

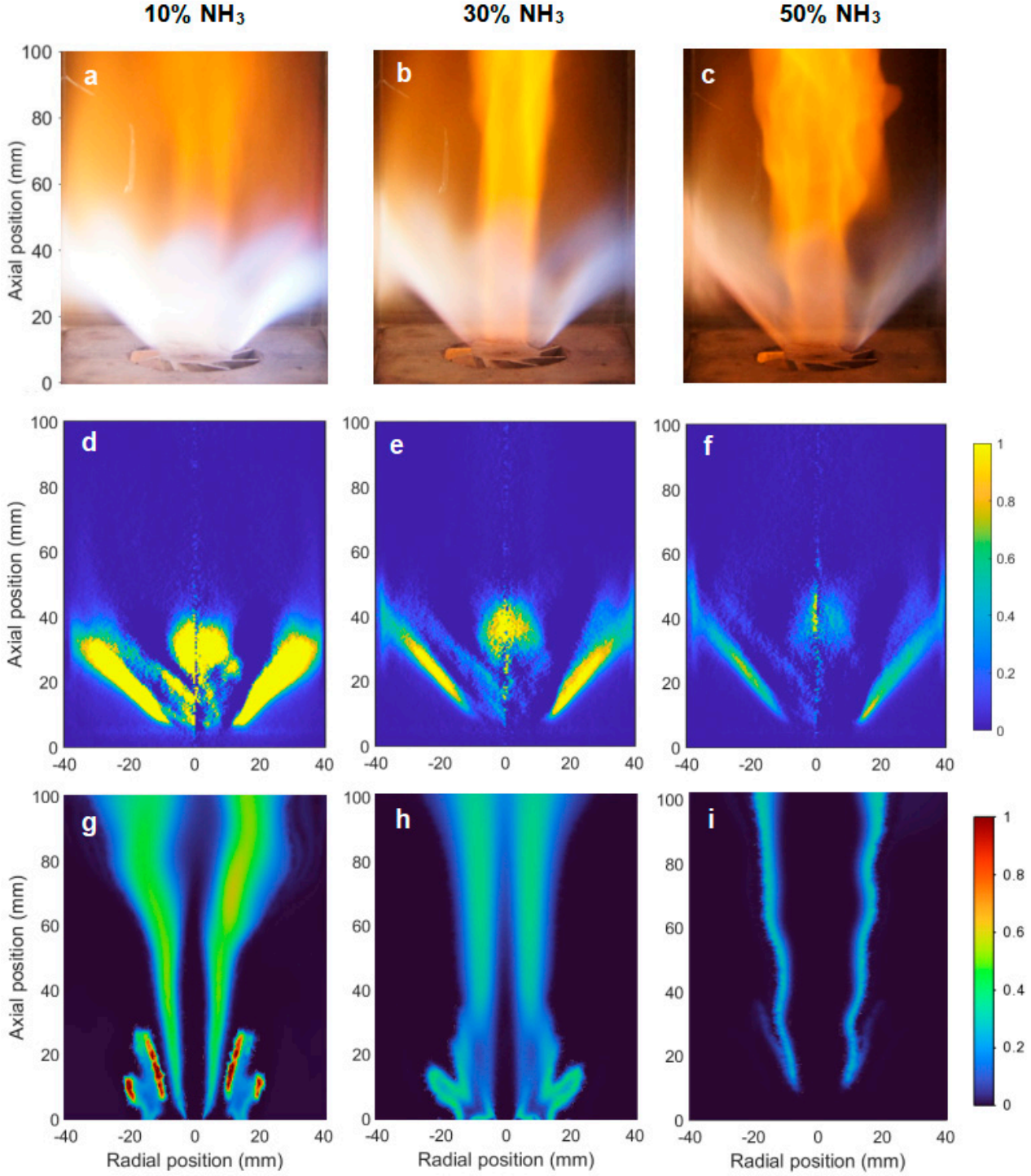

Figure 6. Dual flame images (**a**–**c**) and OH* Abel inversion results (**d**–**f**) and CFD simulated OH mass fraction (**g**–**i**), ϕ = 0.7, with different NH_3/CH_4 vol.%.

As shown in Figure 6d–f, the intensity of the OH* heat release region significantly decreases with increasing NH_3 percentages. Compared to the premixed flame under similar operating conditions, the reduction in OH* chemiluminescence intensity is particularly pronounced. Furthermore, the numerical simulation results presented in Figure 6g–i provide a more detailed distribution of OH within the flame. When the NH_3 percentage is at 10%, a significant presence of OH can be observed in the outer swirl, along with a minor distribution in the central jet flame. As the NH_3 percentage increases, the methane proportion in the outer swirl decreases, reducing the OH distribution in the outer swirl, leaving only a small amount observed at the periphery of the jet flame.

From the numerical simulation, the temperature contour plots of the premixed flame presented in Figure 7a–c, reveal a gradual decrease in the central flame temperature at an equivalence ratio (ϕ) of 0.7, as the proportion of NH_3 increases. This is attributed to the lower heating value of NH_3 compared to CH_4. In Figure 7a, where the methane proportion is highest, the temperature at the point of maximum heat release can reach approximately 2000 K. Similarly, Bayramoğlu et al. [24] conducted a numerical study on the combustion effects of methane-hydrogen and methane-ammonia-hydrogen fuel mixtures on system performance and emissions. The study first examined the effects of methane mixed with 5%, 10%, and 15% hydrogen, followed by an investigation of methane mixed with a fixed 5% hydrogen and 5%, 10%, and 15% ammonia. The results indicated that adding 15% ammonia led to a temperature drop of 200 K and a slight shift in the peak temperature location away from the injection point. As the NH_3 mass fraction increased, the flame temperature at $x/d > 0.4$ decreased slightly. This occurs due to the lower energy release and intensity of ammonia combustion, resulting in lower diffusivity compared to hydrogen and methane. The results also showed that with a constant hydrogen fraction, increasing the ammonia fraction reduced the maximum combustion temperature. Although the general shape of the flame distribution remained similar for all mixtures, the maximum temperature zone became smaller as the ammonia content increased.

From the temperature contour plots of the dual flame in Figure 8a, the highest flame temperature occurs at the swirl flame, due to the high methane proportion of 90%. As the NH_3 proportion in the central jet flame increases to 50%, the central jet flame exhibits a higher temperature, since the nitrogen oxides produced by NH_3 maintain the temperature at approximately 2000 K. This trend is also evident from the actual flame images, where the intensity of the swirl flame gradually decreases with the increase in NH_3 proportion, while the central jet flame exhibits a more pronounced bright yellow flame.

Research conducted by Bazooyar et al. [25] compared the combustion characteristics of ammonia with traditional fuels such as natural gas and hydrogen under the conditions of a 12 kW turbine and a 45 kW boiler. The study analyzed the combustion properties of ammonia, including adiabatic flame temperature and laminar flame speed. Numerical modeling and analysis of ammonia combustion in conventional boiler and turbine combustors were performed. The results indicated that ammonia's combustion temperature could reach up to 2400 K, demonstrating that ammonia can achieve high temperatures during combustion. The combustion temperature is similar to that of methane fuel, but the highest spatial temperature region remains between the primary and secondary holes. Due to the high mass flow rate and low heating value of ammonia, its combustion is more intense in both the primary and secondary regions, resulting in more pronounced high-temperature areas. Additionally, the high combustion temperature of ammonia leads to increased NO_x emissions. The likelihood of NO_x formation is particularly high at elevated spatial temperatures.

Figure 9 compares the temperature contour plots at different heights for premixed and dual flames with 30% NH_3. The temperature contours are taken at H = 10, 20, and 30mm. From the figures, it can be seen that the maximum temperature of the premixed flame is higher than that of the dual flame. However, the high-temperature region of the premixed flame is concentrated at the exit of the swirler and expands with increasing height. In contrast, the dual flame shows an increase in temperature at the swirler exit with

increasing height, but the high-temperature distribution area is smaller than that of the premixed flame. Additionally, it is evident that the high-temperature region of the dual flame resembles the shape of the swirler exit, with the central jet NH_3 flame temperature ranging between 1500 K and 1700 K.

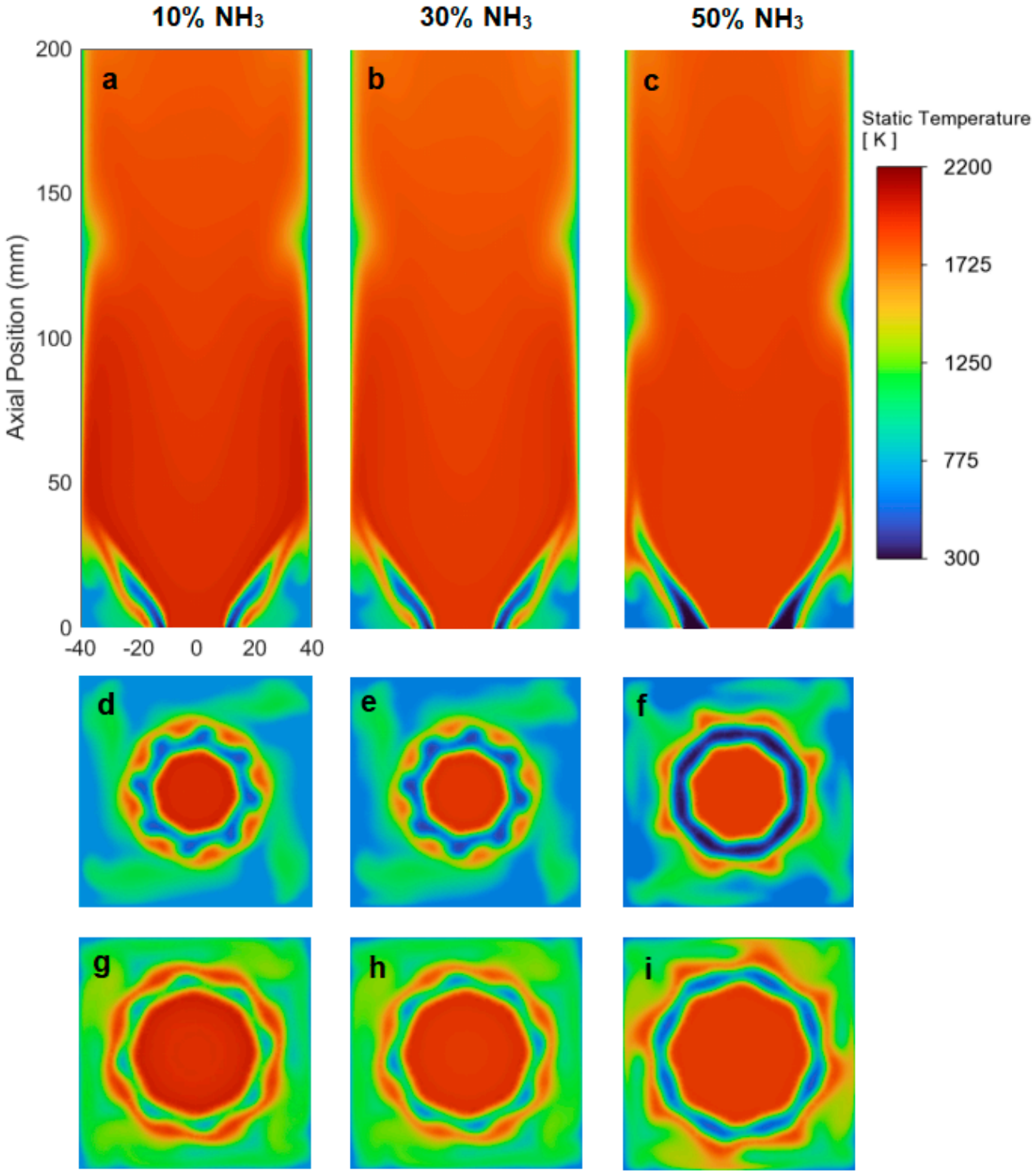

Figure 7. CFD simulated temperature contour plots of premixed flames at ϕ = 0.7, with different NH_3/CH_4 vol.% (**a**–**c**), and contour plots at different heights: H = 10 mm (**d**–**f**) and H = 20 mm (**g**–**i**).

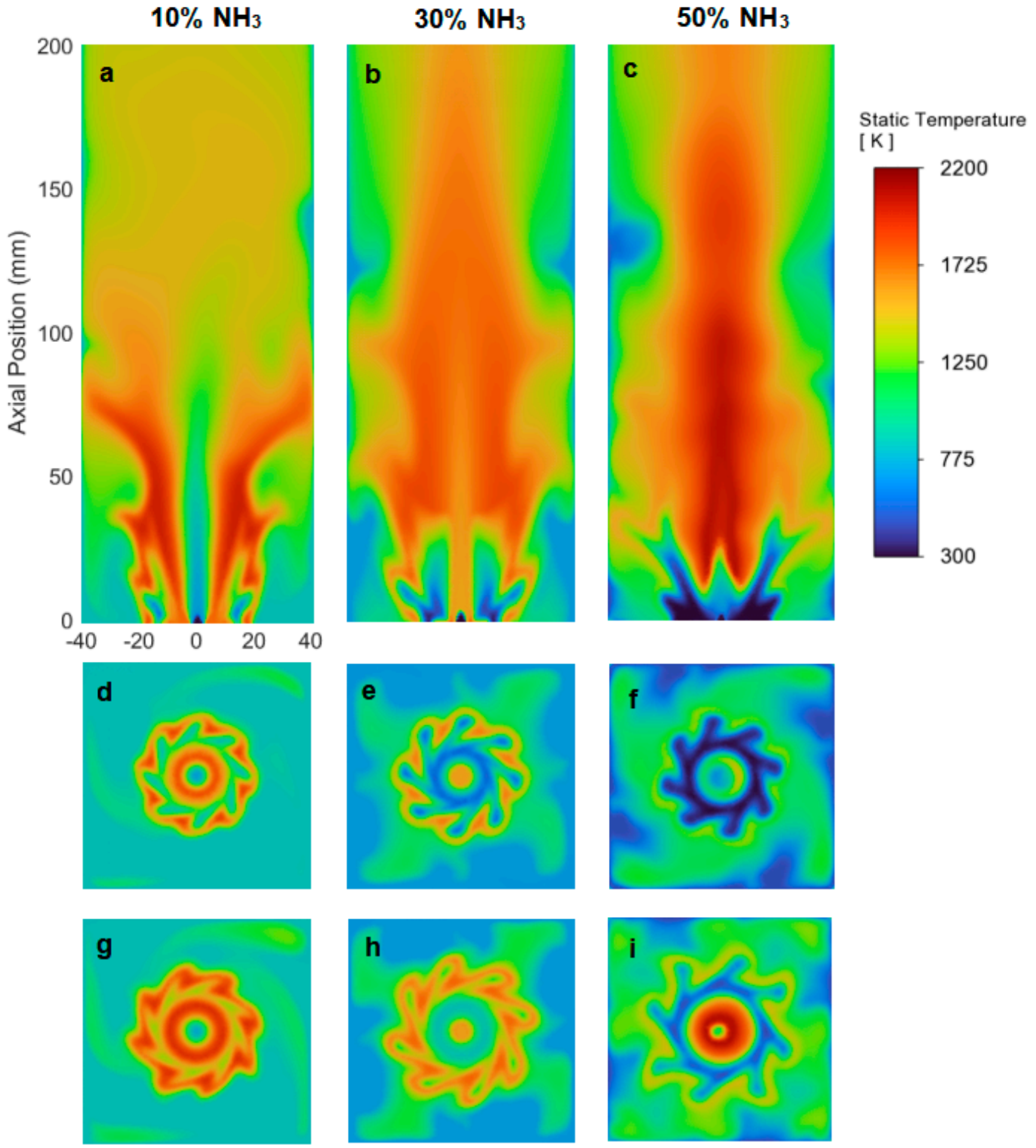

Figure 8. CFD simulated temperature contour plots of dual flames at ϕ = 0.7, with different NH_3/CH_4 vol.% (**a**–**c**), and contour plots at different heights: H = 10 mm (**d**–**f**) and H = 20 mm (**g**–**i**).

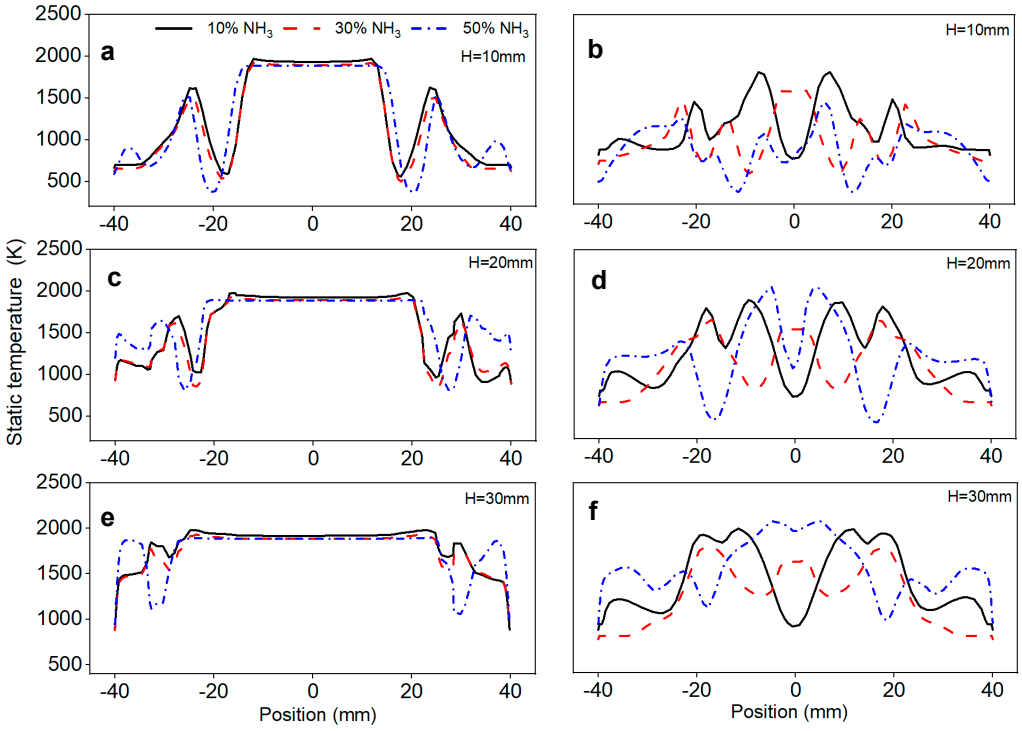

Figure 9. Temperature cross-section profiles of premixed flames (**a**,**c**,**e**) and dual flames (**b**,**d**,**f**) at different heights under ϕ = 0.7, with different NH_3/CH_4 vol.%.

From Figure 9, the left column shows the temperature profiles of premixed flames at different heights. It can be observed that with an increase in the NH_3 ratio, the changes in the high-temperature region in the middle are not significant, only slightly decreasing. However, the temperature fluctuations at the swirl exit are more pronounced. At H = 30 mm, it is evident that when the NH_3 ratio is 50%, the flame temperature is significantly lower at approximately 0.35 m from the center compared to NH_3 ratios of 10% and 30%. Combined with Figure 7, it is apparent that the height of the swirl flame changes, with the highest heat release region moving towards the exit and simultaneously approaching the wall.

The right column presents temperature cross-sectional images of the dual flame at various heights. It can be observed that with the NH_3 ratio increasing from 10% to 50%, the temperature fluctuations of the central jet flame become more pronounced. At H = 10 mm, the central jet flame temperature is highest at 30% NH_3. However, as H increases to 30 mm, the temperature reaches its maximum at 50% NH_3. Additionally, at the outer swirl flame (position 20–40 mm), it is evident that the flame temperature for 10% NH_3 does not vary significantly with different heights (H). However, as the NH_3 ratio increases to 50%, the flame temperature reaches a relatively high value, approximately 1500 K, while the peak temperature of the central jet flame is around 2000 K.

3.2. Combustor Flow Field

Figure 10 illustrates the distribution of velocity vector fields for premixed combustion and dual flame combustion. A comparison between the results of PIV experiments and CFD calculations reveals the distribution of internal and external circulation zones under two different combustion modes.

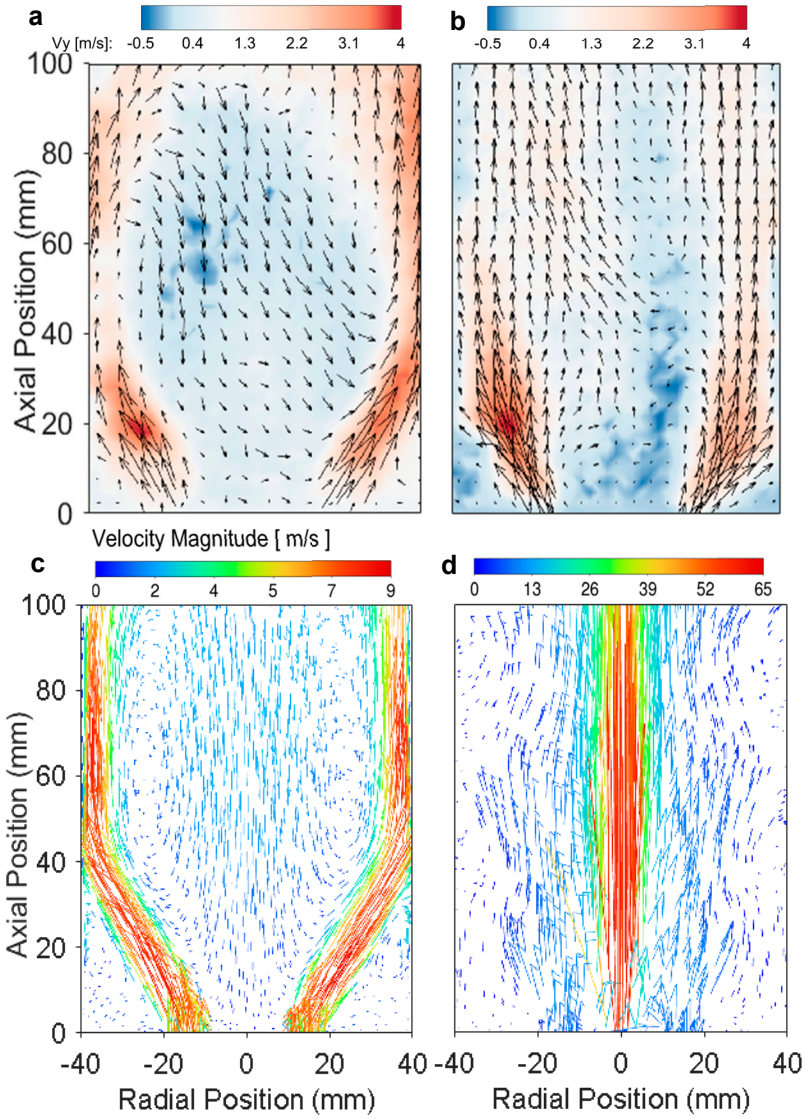

Figure 10. PIV flow field images of (**a**) premixed flames and (**b**) dual flames and the respective simulated flow field contour plots (**c**,**d**), established at ϕ = 0.7, 30% NH_3/70% CH_4.

The flame flow field of swirling combustion is significantly influenced by chemical reactions. Figure 10a,c depict the average velocity vector fields of premixed flames, exhibiting typical CRZ and outer recirculation zones. The flow field affects flame structure and stability, with the recirculation zones providing critical stabilization mechanisms by transporting high-temperature flue gas to the base of the flame, thereby enhancing the mixing process [26].

Figure 10b,d illustrate that the dual flame exhibits a flow field different from that of the premixed flame. In the vicinity of the jet flame region, the injection of air and fuel forms a high-speed region and a recirculation zone between the wall, enhancing mixture mixing. This effect is primarily attributed to the recirculation zones within the burner, which bring both unburned and burned gases into the combustion chamber, thereby enhancing flame stability. The center jet velocity is 4–5 times higher than the swirl velocity, thereby forming a high shear layer between the stratified flames. It is to be noted that the center jet flow is not seeded with tracing particles, hence the flow vectors at the center region of the dual flame are not clearly evident in the PIV-measured flow field (Figure 10b).

Figure 11 shows the velocity contour maps of the premixed and dual flames, revealing significant differences in velocity distribution between the two combustion modes. In Figure 11a–c, it can be observed that with an increasing NH_3 ratio, the velocity peak of

the premixed flame gradually decreases, and a noticeable recirculation zone appears. In Figure 11d–f, it is evident that as the NH_3 ratio increases, the velocity of the central jet flame gradually increases, resulting in a higher flame height.

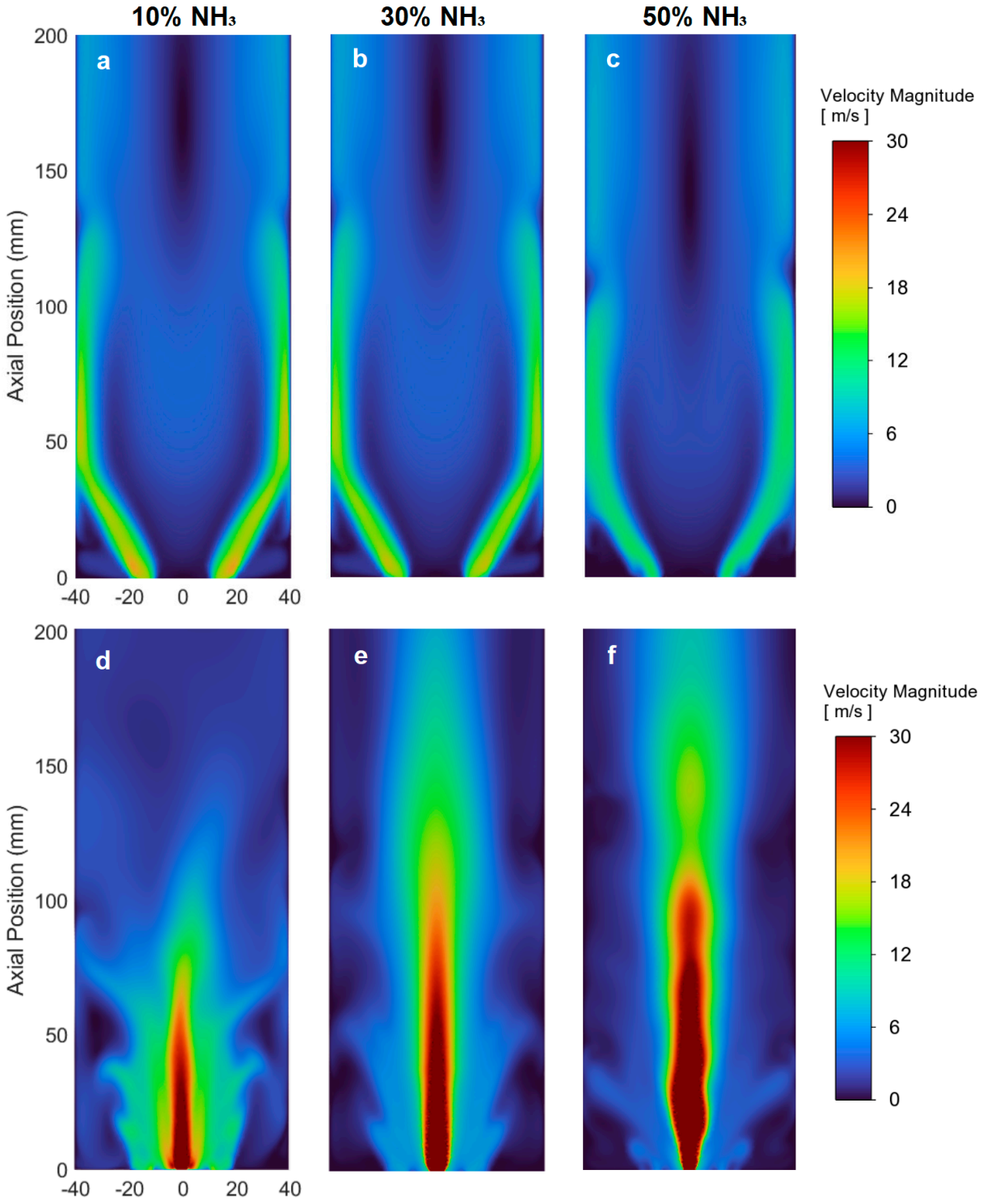

Figure 11. Velocity contours of premixed flame (**a**–**c**) and dual flame (**d**–**f**) under $\phi = 0.7$, with different NH_3/CH_4 vol.%.

Figure 12 compares PIV measurements and simulation results at different heights from 10 mm to 30 mm. The absence of tracer particles in the central jet flame of the dual flame results in the flow velocity in the central area not being captured, leaving it blank

and focusing solely on the comparison of the axial velocity field of the outer swirling flow. During data processing, all data were normalized to maintain consistency between CFD and PIV comparisons [27].

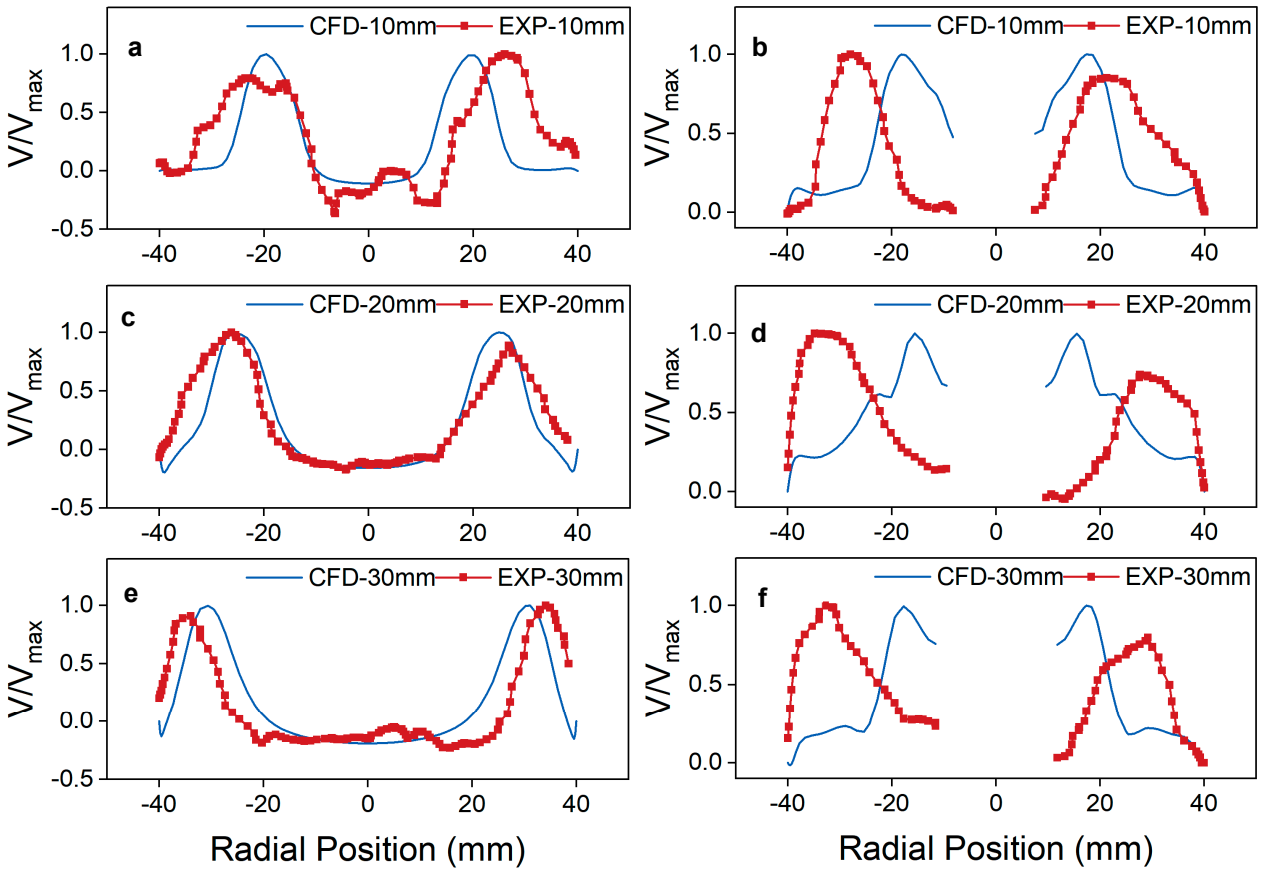

Figure 12. Comparison of experimental and CFD simulated axial velocity cross-section profiles of premixed flames (**a**,**c**,**e**) and dual flames (**b**,**d**,**f**) at H = 10, 20, and 30 mm, with ϕ = 0.7 for a 30% NH_3/70% CH_4.

In Figure 12, solid lines represent CFD simulation results, which fit well with experimental data at peak velocity positions. Areas with negative axial velocity can be defined as recirculation zones, with recirculation velocity increasing closer to the exit of the combustion chamber. The peak velocity of the dual flame is slightly higher than that of the premixed flame. From H = 10 mm to 30 mm, the radial width of the central recirculation zone in the premixed flame increases and approaches the wall, exhibiting a similar trend in the dual flame. The blank area in the middle of the dual flame corresponds to the ammonia jet flame, where no tracer particles were injected, and thus this area was left blank. For normalization purposes and to facilitate better comparison with the experimental data, the CFD results were also left blank in this region.

3.3. NO Emissions and Formation Kinetics

Figure 13 presents the distributions of NH_2 chemiluminescence and the thermal NO and prompt NO results from CFD simulations for both premixed flames and dual flames. As observed in Figure 13a,b, NH_2 exhibits distinctly different distributions; it is predominantly present in the swirl flame of the premixed configuration, while in the dual flame, it primarily accumulates in the jet flame, with a minor presence in the outer swirl.

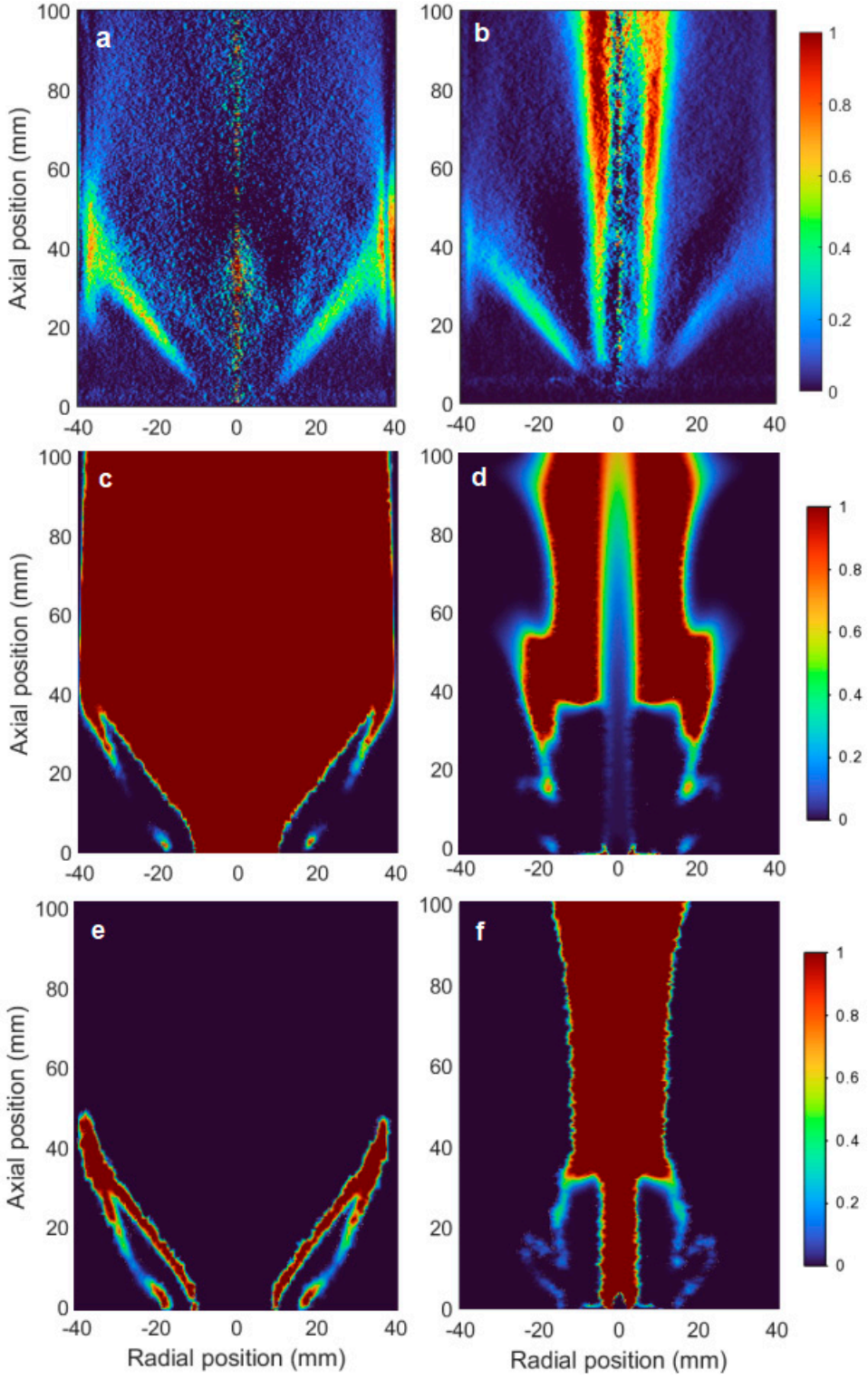

Figure 13. Comparison of experimental NH_2* chemiluminescence Abel inversion (**a**,**b**) and CFD simulated thermal NO (**c**,**d**) and prompt NO (**e**,**f**) for premixed and dual flames, with ϕ = 0.7 for a 30% NH_3/70% CH_4.

Additionally, Figure 13c,d illustrate the distribution of thermal NO, which is more extensive in the premixed flame. In the premixed configuration, thermal NO is mainly concentrated around the periphery of the jet flame, with significantly less presence in the outer swirl. Furthermore, Figure 13e,f reveal that prompt NO in the premixed flame is primarily distributed at the tail and root of the flame, while in the dual flame, prompt NO

is concentrated in the jet flame, exhibiting a smaller spatial range compared to thermal NO, with only a minor presence detected in the outer swirl.

From Figure 13, it can be observed that the prompt NO contour plots show significantly higher values for the dual flame compared to the premixed flame. However, the thermal NO contour plots exhibit the opposite trend, with the premixed flame showing much higher values than the dual flame. Similarly, An et al. [5] found in experimental and numerical simulation studies of NH_3/CH_4 swirl combustion that NO generation peaks when the NH_3 fraction approaches 40%, indicating a significant impact of the NH_3 ratio on NO formation. Additionally, NO generation is positively correlated with temperature, with higher temperatures leading to increased NO concentrations, highlighting the importance of high temperatures in promoting NO formation. In premixed CH_4/NH_3/air flames, NO formation is positively correlated with OH concentrations. Furthermore, HNO plays a crucial role as an intermediate species in the NO formation process, with its presence significantly influencing NO concentrations. The generation of NO is associated with a series of temperature-dependent chemical reactions, particularly the extended Zeldovich mechanism, which involves HNO. N_2O formation is related to NH radicals, with NH radicals playing a key role in N_2O formation through the reaction NO + NH → N_2O + H.

Figure 14 compares the experimental and numerical simulation results of NO emissions at ϕ = 0.7. As shown, the experimental results indicate that the NO emission values of the dual flame are lower than those of the premixed flame. As the NH_3 proportion increases, the NO emission values increase, following the same trend for both premixed and dual flames. From the numerical simulation results, it can be seen that the NO emissions of the premixed flame are similar at an NH_3 proportion of 10%. However, as the NH_3 proportion increases, the NO emissions of the premixed flame increase significantly, whereas the NO emissions of the dual flame slightly increase at an NH_3 proportion of 30% and slightly decrease at 50%. This discrepancy may be attributed to the influence of environmental factors and discrepancies between actual combustion and numerical simulation. The overall trend is consistent, indicating that NO emissions of the premixed flame are higher than those of the dual flame under the same operating conditions.

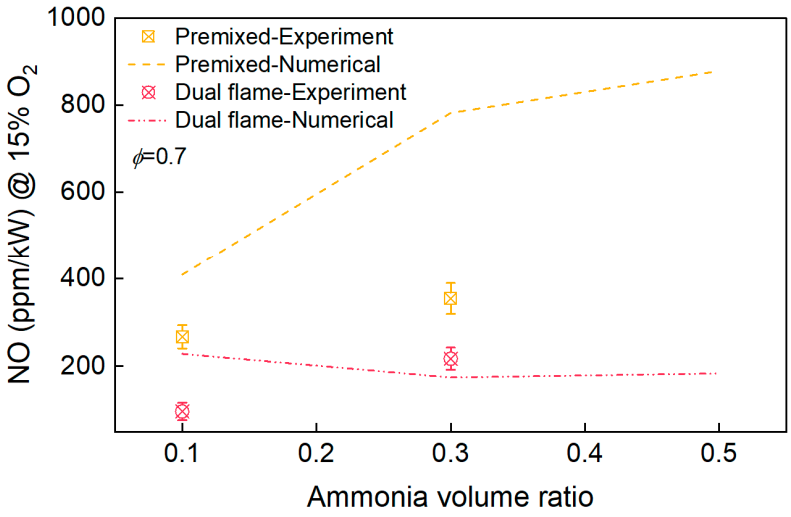

Figure 14. Comparison of experimental and numerical simulation results of NO emissions at ϕ = 0.7 for different NH_3/CH_4 vol.%.

Similarly, Bastani et al. [28] investigated the experimental and numerical simulation of ammonia/methane in a micro-combustor, analyzing NO emissions. The study indicated that as the ammonia fraction in the fuel increased, the flame temperature decreased and the flame moved away from the injector. Additionally, adding ammonia to the fuel seemed to increase the NO_x production within the combustor. Although the exit temperature of the combustor remained almost constant, the combustion efficiency decreased with the increas-

ing ammonia fraction. The study also found that ammonia undergoes dehydrogenation by OH^*, forming NH_2 and NH, initiating the NO formation pathway. The oxidation of NH with O_2 produces HNO and NO, ultimately generating NO through different pathways. The oxidation pathways of carbon and nitrogen species are different, but the formation of NO_x relies on the oxidation of ammonia. NH_3 primarily oxidizes through high-temperature branching reactions of H_2/O_2, producing OH and HO_2 radicals. Ammonia more readily consumes OH^* than methane, increasing NO formation. OH^* plays a crucial role in NO_x formation, significantly elevating NO_x emissions even at low ammonia concentrations.

Previously, Füzesi et al. [29] investigated the transient and steady-state results of experimental and numerical simulations of ammonia and methane in a swirling flame. The study shows that with 20% ammonia, the maximum deviation in NO emissions estimated by steady-state simulations is 622.1 ppm. The lowest NO emissions occur with pure methane, at 15.9 ppm, and with 50% ammonia, the emissions are 18.8 ppm. Except for the 20% ammonia mixture, the relative difference in NO emissions among the fuel mixtures remains around 5%.

3.4. Sensitivity Analysis

Figure 15 illustrates the sensitivity analysis of NO formation in premixed and dual flames as a function of the NH_3 ratio. As shown in Figure 15a, for the premixed flame, the reaction $NH_2 + O \leftrightarrow HNO + H$ has the highest sensitivity coefficient, which is positive and represents the consumption of NH_2. The sensitivity coefficient increases significantly with the NH_3 ratio, being approximately 6.7 times higher at 50% NH_3 compared to 10% NH_3. Additionally, the reaction $N_2O + O \leftrightarrow 2NO$ also exhibits a high sensitivity coefficient, indicating that NO formation is significantly influenced by the increase in NH_3 ratio, with the oxidation reaction rate increasing markedly. Conversely, the reaction $N_2O + H \leftrightarrow N_2 + OH$ is inhibited, leading to a decrease in OH formation as the NH_3 ratio increases and the CH_4 ratio decreases. Furthermore, several key reactions that inhibit NO reduction include $NH_2 + NO \leftrightarrow NNH + OH$, $NH + NO \leftrightarrow N_2O + H$, and $NH + NO \leftrightarrow N_2 + OH$. It is evident that with an increasing NH_3 ratio, the reaction rates of NO consumption decrease, resulting in higher sensitivity coefficients for NO inhibition.

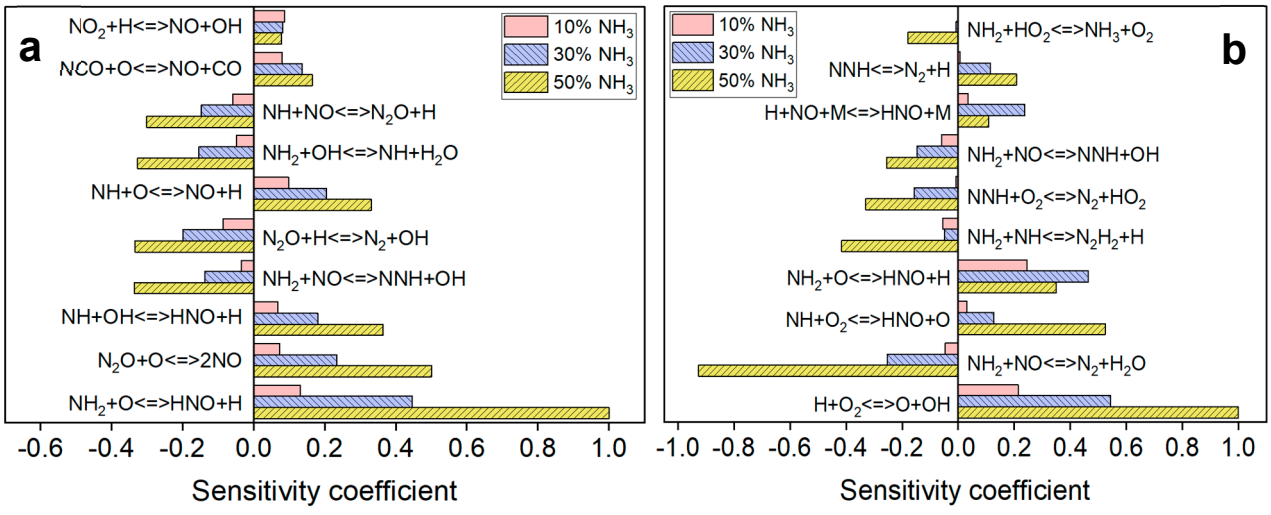

Figure 15. Analysis of NO sensitivity coefficients for different NH_3/CH_4 vol.% flames established at ϕ = 0.7, under (**a**) premixed and (**b**) dual flame modes.

In contrast to the premixed flame, as shown in Figure 15b, the reaction $NH_2 + O \leftrightarrow HNO + H$ is not the most significant consumption reaction in the dual flame. It is evident that the reaction rate does not change significantly when the NH_3 ratio increases from 30% to 50%, but the sensitivity coefficient at 50% NH_3 is twice that at 10% NH_3. The reaction H

+ O_2 ↔ O + OH has the highest sensitivity coefficient in dual flame combustion, and the rate of OH formation increases significantly with the NH_3 ratio.

Additionally, the reaction NH_2 + NO ↔ N_2 + H_2O is a highly sensitive NO reduction reaction. As the NH_3 ratio increases, this reaction becomes more significantly inhibited, leading to a decreased NO consumption rate similar to the results observed in the premixed flame. Furthermore, in the sensitivity coefficient analysis of the reaction NH_2 + NO ↔ NNH + OH, it can be seen that when the NH_3 ratio increases to 50%, the sensitivity coefficient is positive, differing from the results at 10% and 30% NH_3. This indicates that with a 50% NH_3 ratio, the reaction shifts from inhibition to the consumption of NO, unlike in the premixed flame, where NO inhibition occurs at all three NH_3 ratios.

Figure 16 presents a comparative sensitivity analysis of NO_2 for both premixed flames and dual flames. As shown in Figure 16a, the most prominent reaction sensitivity in the premixed flame is the promoting reaction NO + O + M ↔ NO_2 + M. As the NH_3 ratio increases and the CH_4 ratio decreases, the sensitivity of this reaction gradually diminishes, indicating a reduction in NO consumption and an increase in NO levels. Conversely, the reaction NO_2 + H ↔ NO + OH is inhibitory, with the consumption of NO_2 accelerating as the NH_3 ratio increases, thereby increasing the NO generation rate. Notably, in the reaction OH + HO_2 ↔ O_2 + H_2O, the inhibition of OH consumption shows a decrease followed by an increase as the NH_3 percentage rises from 10% to 50%, suggesting that the reaction rate initially decreases before subsequently increasing, leading to a change in the reduction reaction of OH.

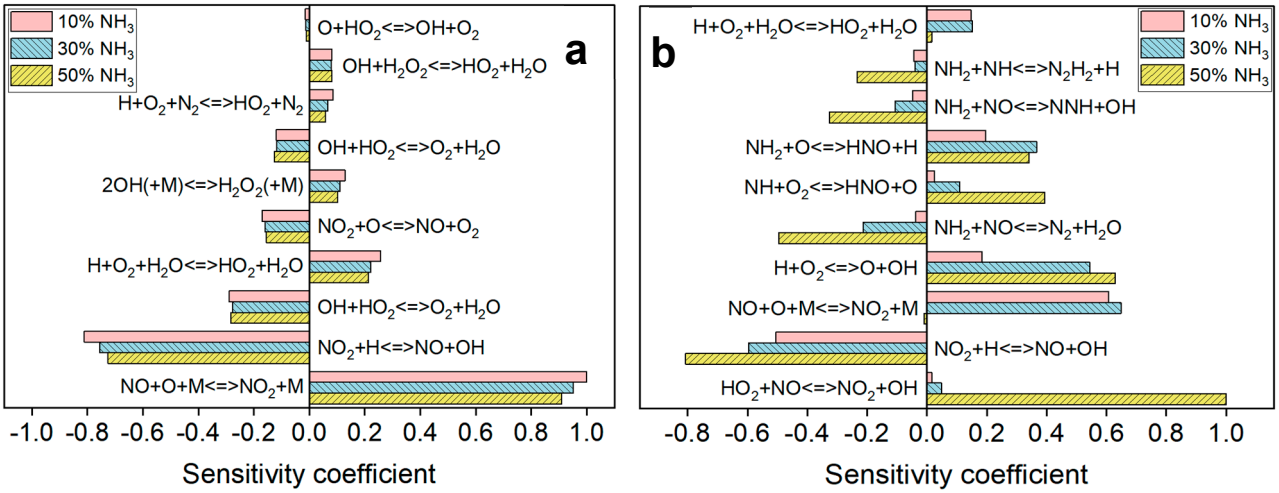

Figure 16. Analysis of NO2 sensitivity coefficients for different NH_3/CH_4 vol.% flames established at ϕ = 0.7, under (**a**) premixed and (**b**) dual flame modes.

Furthermore, as depicted in Figure 16b, the most significant sensitivity in the dual flame occurs in the reaction HO_2 + NO ↔ NO_2 + OH. As the NH_3 ratio increases from 10% to 30%, there is a minor enhancement in the reaction rate; however, when the ratio rises from 30% to 50%, the consumption reaction of NO exhibits a marked increase, indicating a substantial enhancement in the reaction rate for NO_2 generation. Additionally, the reaction NO_2 + H ↔ NO + OH shows a negative sensitivity coefficient, indicating an inhibitory reaction. As the NH_3 ratio increases, the sensitivity coefficient increases, suggesting that the consumption of NO_2 in this reaction becomes progressively inhibited, thereby weakening the generation of NO and OH. Moreover, the sensitivity coefficient for the reaction NH_2 + NO ↔ N_2 + H_2O is also negative, indicating that the production of N_2 is suppressed in this context, and as the NH_3 ratio increases, the coefficient rises, suggesting an increase in NO.

Figure 17 illustrates the comparison of global sensitivity coefficients for premixed flames and dual flames. In Figure 17a, it is evident that the most significant overall

reaction in the premixed flame is OH + C_2H_6 ↔ C_2H_5 + H_2O, with a negative sensitivity coefficient indicating that the consumption of OH is suppressed in this reaction. As the NH_3 percentage increases from 10% to 50%, the sensitivity coefficient increases by approximately 20 times, demonstrating a pronounced impact of NH_3 on this reaction.

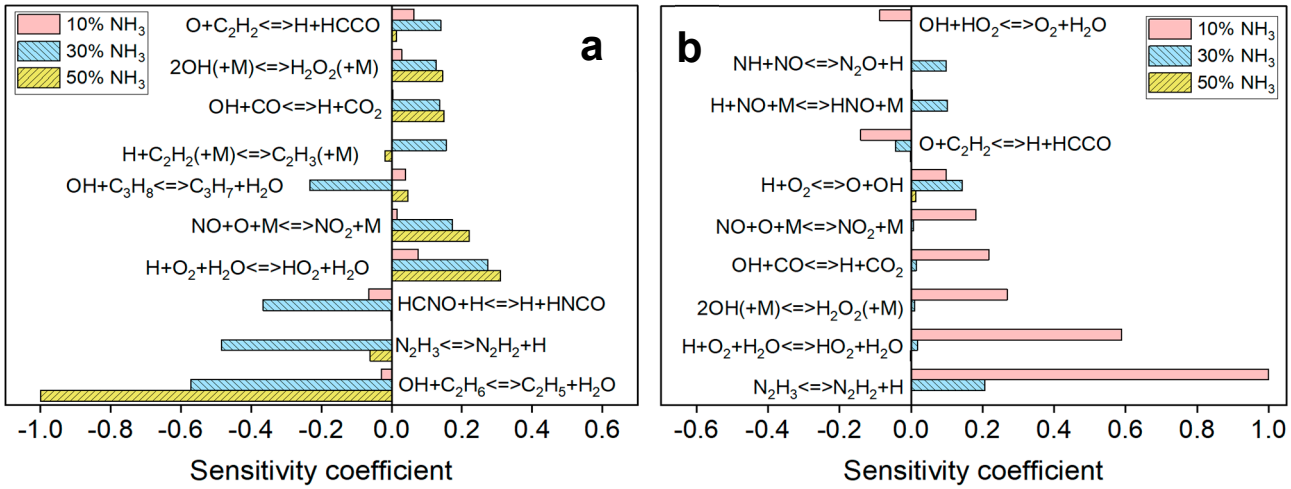

Figure 17. Analysis of global sensitivity coefficients for different NH_3/CH_4 vol.% flames established at ϕ = 0.7, under (**a**) premixed and (**b**) dual flame modes.

Additionally, for the reaction N_2H_3 ↔ N_2H_2 + H, the premixed and dual flames exhibit opposite trends. In Figure 17a, this reaction shows a negative coefficient, while in Figure 17b, it displays a positive coefficient, indicating that it is the strongest reaction in terms of sensitivity in the dual flame scenario. At an NH_3 percentage of 10%, its sensitivity coefficient is roughly five times that at 30%; however, as the NH_3 percentage increases to 50%, the sensitivity coefficient significantly decreases, nearly negligible compared to the 10% case, suggesting that the consumption of N_2H_3 diminishes with higher NH_3 percentages. Conversely, in the premixed flame, the sensitivity coefficient decreases as the NH_3 percentage increases, indicating that the generation of N_2H_2 is suppressed, becoming nearly insignificant at 10% NH_3.

Moreover, the reaction H + O_2 + H_2O ↔ HO_2 + H_2O exhibits similar trends in both premixed and dual flames, both acting as promoting consumption reactions. However, the sensitivity coefficient in the premixed flame increases with rising NH_3 percentages, showing a minor increase from 30% to 50%. In the dual flame scenario, the sensitivity coefficient is highest at an NH_3 percentage of 10%, and it approaches zero as the percentage increases to 50%, indicating that higher NH_3 concentrations reduce the consumption of this reaction and decrease the reaction rate.

In summary, the sensitivity of the OH formation reaction H + O_2 ↔ O + OH significantly increases in the dual flame, promoting the formation of OH, which primarily reacts with NO to form NO_2, a process that is relatively independent of NO generation. In contrast, in the premixed flame, the reaction NH_2 + O ↔ HNO + H contributes significantly to NO formation. As the NH_3 ratio increases, the sensitivity of this reaction rises significantly, leading to a marked increase in NO generation. Additionally, in the dual flame, as the NH_3 ratio increases, the sensitivity of the reaction HO_2 + NO ↔ NO_2 + OH significantly increases, enhancing NO_2 formation. The formation of NO_2 consumes some NO, thereby reducing NO concentrations. In comparison, this reaction has a weaker influence on NO_2 in the premixed flame.

4. Conclusions

Although ammonia combustion faces challenges concerning NO_x emissions and flame stability, careful optimization of fuel blending and combustion parameters can significantly

enhance its performance. In this research, we explored and contrasted two unique fuel injection methodologies: one involving ammonia and methane in both a fully premixed and swirl configuration, and another employing a dual flame combustion approach, where a central ammonia/air jet flame operates alongside a coflow methane/air flame in swirl mode. The principal outcomes of this study are summarized as follows:

1. Increasing the NH_3 ratio leads to a slight reduction in the high-temperature region of the premixed flame, with more pronounced temperature fluctuations at the swirler exit. When the NH_3 ratio reaches 50%, a significant drop in flame temperature is observed, particularly at a height of 30 mm.
2. As the NH_3 ratio increases, temperature fluctuations in the central jet flame become more pronounced. The maximum temperature shifts to the 50% NH_3 condition with increasing height, while temperature variations in the outer swirl flame remain relatively minor across different heights.
3. Numerical simulation results align closely with PIV measurements at peak velocity positions. Negative axial velocities indicate recirculation zones, with recirculation velocity increasing near the combustion chamber exit.
4. Prompt NO levels are higher in the dual flame compared to the premixed flame. Conversely, the thermal NO levels are significantly higher in the premixed flame than in the dual flame.
5. The NO emission values for the dual flame are lower than those for the premixed flame. Both types of flames exhibit an increase in NO emissions with increasing NH_3 proportion.
6. In the dual flame, the $NH_2 + O \leftrightarrow HNO + H$ reaction is less significant compared to the premixed flame, while the $H + O_2 \leftrightarrow O + OH$ reaction shows the highest sensitivity coefficient. As the NH_3 proportion increases, the rate of NO consumption reactions decreases, resulting in a higher sensitivity coefficient for NO inhibition.

This study focuses on the development and implementation of a dual-flame combustion strategy aimed at enhancing ammonia combustion performance while reducing NO_x emissions. By integrating a CRN model with ANSYS Fluent simulations, a framework for optimizing ammonia/methane combustion is established, providing new insights into clean combustion technologies by comprehensively analyzing NO formation and flame dynamics.

The dual-flame combustion strategy and the corresponding simulation model have significant potential for reducing NO_x emissions and improving flame stability in ammonia combustion systems. This methodology is applicable to various industrial sectors, including power generation and industrial heating. Furthermore, the proposed model and methodology are also adaptable to other fuel mixtures and combustion scenarios, offering flexible tools for future research and clean energy technologies.

Author Contributions: Conceptualization, C.T.C.; methodology, S.W. and C.T.C.; validation, S.S., J.-H.N., A.V.-M. and B.T.; formal analysis, S.W.; investigation, S.W., S.S. and C.T.C.; data curation, S.W.; writing—original draft preparation, S.W.; writing—review and editing, S.S., C.T.C., J.-H.N. and A.V.-M.; supervision, C.T.C.; project administration, C.T.C.; funding acquisition, C.T.C. All authors have read and agreed to the published version of the manuscript.

Funding: The funding from the Science and Technology Commission of Shanghai Municipality (23160712400) is gratefully acknowledged.

Data Availability Statement: The raw data supporting the conclusions of this article will be made available by the authors on request.

Conflicts of Interest: The authors declare no conflict of interest.

References

1. Ilbas, M.; Kumuk, O.; Alabas, B. Experimental investigation of the combustion instability behaviors and NO_x emissions in an ammonia/methane fueled low eddy premixed burner. *J. Energy Inst.* **2023**, *108*, 101241. [CrossRef]
2. Berwal, P.; Kumar, S.; Khandelwal, B. A comprehensive review on synthesis, chemical kinetics, and practical application of ammonia as future fuel for combustion. *J. Energy Inst.* **2021**, *99*, 273–298. [CrossRef]
3. Alnajideen, M.; Shi, H.; Northrop, W.; Emberson, D.; Kane, S.; Czyzewski, P.; Alnaeli, M.; Mashruk, S.; Rouwenhorst, K.; Yu, C.; et al. Ammonia combustion and emissions in practical applications: A review. *Carbon Neutrality* **2024**, *3*, 13. [CrossRef]
4. Jójka, J.; Slefarski, R. Emission characteristics for swirl methane–air premixed flames with ammonia addition. *Energies* **2021**, *14*, 662. [CrossRef]
5. An, Z.; Zhang, M.; Zhang, W.; Mao, R.; Wei, X.; Wang, J.; Huang, Z.; Tan, H. Emission prediction and analysis on CH_4/NH_3/air swirl flames with LES-FGM method. *Fuel* **2021**, *304*, 121370. [CrossRef]
6. Xiao, H.; Valera-Medina, A.; Marsh, R.; Bowen, P.J. Numerical study assessing various ammonia/methane reaction models for use under gas turbine conditions. *Fuel* **2017**, *196*, 344–351. [CrossRef]
7. Tian, Z.; Li, Y.; Zhang, L.; Glarborg, P.; Qi, F. An experimental and kinetic modeling study of premixed $NH_3/CH_4/O_2$/Ar flames at low pressure. *Combust. Flame* **2009**, *156*, 1413–1426. [CrossRef]
8. Okafor, E.C.; Naito, Y.; Colson, S.; Ichikawa, A.; Kudo, T.; Hayakawa, A.; Kobayashi, H. Experimental and numerical study of the laminar burning velocity of CH_4–NH_3–air premixed flames. *Combust. Flame* **2018**, *187*, 185–198. [CrossRef]
9. Ahmed, M.M.A.; Xu, L.; Bai, X.-S.; Hassan, Z.O.; Abdullah, M.; Sim, J.; Cenker, E.; Roberts, W.L.; Elbaz, A.M. Flame stabilization and pollutant emissions of turbulent ammonia and blended ammonia flames: A review of the recent experimental and numerical advances. *Fuel Commun.* **2024**, *20*, 100127. [CrossRef]
10. Mashruk, S.; Alnasif, A.; Yu, C.; Thatcher, J.; Rudman, J.; Peronski, L.; Meng-Choung, C.; Valera-Medina, A. Combustion characteristics of a novel ammonia combustor equipped with stratified injection for low emissions. *J. Ammon. Energy* **2023**, *1*, 21–32. [CrossRef]
11. Wang, S.; Chong, C.T.; Xie, T.; Józsa, V.; Ng, J.-H. Ammonia/methane dual-fuel injection and co-firing strategy in a swirl flame combustor for pollutant emissions control. *Energy* **2023**, *281*, 128221. [CrossRef]
12. Wang, S.; Chong, C.T.; Józsa, V.; Chiong, M.-C. Investigation of NO emissions and chemical reaction kinetics of ammonia/methane flames under dual-fuel co-combustion mode at elevated air temperature conditions. *Int. J. Hydrogen Energy* **2024**, *84*, 968–981. [CrossRef]
13. Ji, L.; Wang, J.; Hu, G.; Mao, R.; Zhang, W.; Huang, Z. Experimental study on structure and blow-off characteristics of NH_3/CH_4 co-firing flames in a swirl combustor. *Fuel* **2022**, *314*, 123027. [CrossRef]
14. Zhang, M.; Wei, X.; Wang, J.; Huang, Z.; Tan, H. The blow-off and transient characteristics of co-firing ammonia/methane fuels in a swirl combustor. *Proc. Combust. Inst.* **2021**, *38*, 5181–5190. [CrossRef]
15. Xie, T.; Chong, C.T.; Wang, S.; Seljak, T.; Ng, J.-H.; Tran, M.-V.; Karmakar, S.; Tian, B. Flow field, flame structure and emissions quantifications of oxygenated glycerol in a swirl flame combustor. *Fuel* **2022**, *321*, 124052. [CrossRef]
16. Yu, H.; Thé, J. Validation and optimization of SST k-ω turbulence model for pollutant dispersion within a building array. *Atmos. Environ.* **2016**, *145*, 225–238. [CrossRef]
17. van Oijen, J.A.; Donini, A.; Bastiaans, R.J.M.; ten Thije Boonkkamp, J.H.M.; de Goey, L.P.H. State-of-the-art in premixed combustion modeling using flamelet generated manifolds. *Prog. Energy Combust. Sci.* **2016**, *57*, 30–74. [CrossRef]
18. Ketelheun, A.; Olbricht, C.; Hahn, F.; Janicka, J. NO prediction in turbulent flames using LES/FGM with additional transport equations. *Proc. Combust. Inst.* **2011**, *33*, 2975–2982. [CrossRef]
19. Füzesi, D.; Wang, S.; Józsa, V.; Chong, C.T. Ammonia-methane combustion in a swirl burner: Experimental analysis and numerical modeling with Flamelet Generated Manifold model. *Fuel* **2023**, *341*, 127403. [CrossRef]
20. Samiran, N.A.; Chong, C.T.; Ng, J.-H.; Tran, M.-V.; Ong, H.C.; Valera-Medina, A.; Chong, W.W.F.; Mohd Jaafar, M.N. Experimental and numerical studies on the premixed syngas swirl flames in a model combustor. *Int. J. Hydrogen Energy* **2019**, *44*, 24126–24139. [CrossRef]
21. Okafor, E.C.; Naito, Y.; Colson, S.; Ichikawa, A.; Kudo, T.; Hayakawa, A.; Kobayashi, H. Measurement and modelling of the laminar burning velocity of methane-ammonia-air flames at high pressures using a reduced reaction mechanism. *Combust. Flame* **2019**, *204*, 162–175. [CrossRef]
22. Mashruk, S.; Kovaleva, M.; Alnasif, A.; Chong, C.T.; Hayakawa, A.; Okafor, E.C.; Valera-Medina, A. Nitrogen oxide emissions analyses in ammonia/hydrogen/air premixed swirling flames. *Energy* **2022**, *260*, 125183. [CrossRef]
23. Da Rocha, R.C.; Costa, M.; Bai, X.-S. Chemical kinetic modelling of ammonia/hydrogen/air ignition, premixed flame propagation and NO emission. *Fuel* **2019**, *246*, 24–33. [CrossRef]
24. Bayramoğlu, K.; Bahlekeh, A.; Masera, K. Numerical investigation of the hydrogen, ammonia and methane fuel blends on the combustion emissions and performance. *Int. J. Hydrogen Energy* **2023**, *48*, 39586–39598. [CrossRef]
25. Bazooyar, B.; Coomson, G.; Manovic, V.; Nabavi, S.A. Comparative analysis of ammonia combustion for domestic applications. *J. Energy Inst.* **2023**, *106*, 101130. [CrossRef]
26. Huang, Y.; Yang, V. Dynamics and stability of lean-premixed swirl-stabilized combustion. *Prog. Energy Combust. Sci.* **2009**, *35*, 293–364. [CrossRef]

27. Sun, Y.; Cai, T.; Shahsavari, M.; Sun, D.; Sun, X.; Zhao, D.; Wang, B. RANS simulations on combustion and emission characteristics of a premixed NH_3/H_2 swirling flame with reduced chemical kinetic model. *Chin. J. Aeronaut.* **2021**, *34*, 17–27. [CrossRef]
28. Bastani, M.; Tabejamaat, S.; Ashini, H. Numerical and experimental study of combustion and emission characteristics of ammonia/methane fuel mixture in micro gas turbine combustor. *Int. J. Hydrogen Energy* **2024**, *49*, 1399–1415. [CrossRef]
29. Füzesi, D.; Józsa, V. The importance of unsteady phenomena of ammonia/methane combustion in an experimental swirl burner: Comparison of steady-state and transient simulation results. *Combust. Flame* **2021**, *227*, 234–249. [CrossRef]